

Recent advances in rigorous computation of Poincaré maps

Tomasz Kapela¹, Daniel Wilczak^{1,*}, Piotr Zgliczyński²

Faculty of Mathematics and Computer Science, Jagiellonian University, Łojasiewicza 6, 30-348 Kraków, Poland.

Abstract

In this article we present recent advances on interval methods for rigorous computation of Poincaré maps. We also discuss the impact of choice of Poincaré section and coordinate system on obtained bounds for computing Poincaré map nearby fixed points.

Keywords: Poincaré map, rigorous numerical analysis, computer-assisted proof

2010 MSC: 65G20,

2010 MSC: 37C27

1. Introduction

Let us consider an ODE

$$x'(t) = f(x(t)), \quad (1)$$

where $f: \mathbb{R}^n \rightarrow \mathbb{R}^n$ is a smooth (in most cases analytic and 'programmable') function, and a local flow $\varphi(t, x)$ induced by (1). The dynamics of continuous time systems can be efficiently studied by reduction to discrete time systems by introducing Poincaré sections and associated Poincaré maps. Such an approach is proved to be very efficient in studying periodic orbits, chaotic horseshoes, chaotic attractors, invariant tori and connecting orbits [1, 2, 3, 4, 5, 6, 7, 8, 9, 10, 11, 12, 13] or analysis of hybrid systems [14, 15, 16, 17].

Informally, a Poincaré map $\mathcal{P}: \Pi_1 \rightarrow \Pi_2$ assigns to a point $x \in \Pi_1$ the first intersection of its trajectory with Π_2 , provided it exists — precise definitions will be given in Section 1.1. There are various rigorous ODE solvers [18, 19, 20, 21, 22, 23] which compute enclosures of the solutions to IVPs. Based on them, one can implement an algorithm for computation of $\mathcal{P}(X)$, where $X \subset \Pi_1$. To the best of our knowledge, the CAPD::DynSys library [18, 19] is the only freely available software that directly supports computation of enclosures of Poincaré maps.

The aim of this paper is to present recent advances in computation of Poincaré maps already implemented in CAPD::DynSys, for which the authors of this article are the main developers. We would like to discuss various aspects that impact obtained enclosures and reduce unavoidable overestimation. In particular, we would like to address the following questions.

*Corresponding author.

Email addresses: Tomasz.Kapela@uj.edu.pl (Tomasz Kapela), Daniel.Wilczak@ii.uj.edu.pl (Daniel Wilczak), Piotr.Zgliczynski@ii.uj.edu.pl (Piotr Zgliczyński)

¹This research is partially supported by the Polish National Science Center under Maestro Grant No. 2014/14/A/ST1/00453.

²This research is partially supported by the Polish National Science Center under Grants No. 2019/35/B/ST1/00655 and UMO-2016/22/A/ST1/00077.

- What is the optimal choice (in the sense of obtained enclosures) of a Poincaré section near a periodic orbit?
- If the sections are fixed (like guards in hybrid systems), can we reduce overestimation by appropriate choice of coordinates on these sections?
- Can we take advantage from the knowledge on internal representation of the solution to IVP in a rigorous ODE solver to reduce overestimation in computation of Poincaré maps?

The article is organized as follows. In Section 2 we discuss our main algorithm and in Section 3 we discuss the questions listed above and report on multiple numerical experiments.

1.1. Notation and basic definitions.

An interval arithmetic is a base for rigorous numerical methods described in this paper. We denote intervals and vectors and matrices with interval entries using bold face letters e.g. \mathbf{x} , \mathbf{X} . The interval hull of a set S , that is the smallest Cartesian product of closed intervals that contains S , is denoted by $[S]_I$. For a function $f: \mathbb{R}^n \rightarrow \mathbb{R}^m$ by $[f]$ we denote its (fixed) realisation in interval arithmetics, that is for $X \subset \mathbb{R}^n$ there holds $f(X) \subset [f](X)$ provided the left hand side exists.

In what follows by $\varphi(t, x)$ we denote a local flow induced by (1) with smooth vector field f .

For a matrix A by A^T we will denote the transposition of A .

For a submanifold M of \mathbb{R}^n and $y \in M$ by $T_y M \subset \mathbb{R}^n$ we will denote the tangent space to M at y .

Throughout the paper for a scalar function $\alpha: \mathbb{R}^n \rightarrow \mathbb{R}$ the derivative $D\alpha(x)$ is the 1-form on $T_x \mathbb{R}^n = \mathbb{R}^n$. It can be represented as

$$D\alpha(x) = \left(\frac{\partial \alpha}{\partial x_1}(x), \dots, \frac{\partial \alpha}{\partial x_n}(x) \right).$$

This is a "row vector" as opposed of $\nabla \alpha(x) = (D\alpha(x))^T$, which is a "column vector". In fact the notion of $\nabla \alpha(x)$ depends on the scalar product, which is silently assumed to be $\langle x | y \rangle = \sum_i x_i y_i$, hence is not independent from the coordinate system.

To denote the application of 1-form w to a vector v we will use the following notation

$$w(v) = \langle w | v \rangle. \quad (2)$$

Usually in the text we will write vectors as $x = (x_1, \dots, x_n)$, i.e. as a row. However in the formulas we will carefully distinguish between vectors as columns and 1-forms as rows.

A 1-form $w: \mathbb{R}^n \rightarrow \mathbb{R}$, $w \neq 0$ will be called a left-eigenvector of a matrix $A \in \mathbb{R}^{n \times n}$ if there exists $\lambda \in \mathbb{C}$, such that

$$A^* w = \lambda w, \quad (3)$$

where A^* denotes the adjoint operator. When $w = (w_1, \dots, w_n)$ in the dual base, then (3) is equivalent to

$$A^T w^T = \lambda w^T. \quad (4)$$

It is well known that A^* and A have the same spectrum and if λ is an eigenvalue of multiplicity 1 with corresponding eigenvector v and the left-eigenvector w , then

$$\langle w | v \rangle \neq 0. \quad (5)$$

Moreover, if w_1 is a left-eigenvector with eigenvalue λ_1 and v_2 is an eigenvector with eigenvalue λ_2 , and $\lambda_1 \neq \lambda_2$, then

$$\langle w_1 | v_2 \rangle = 0. \quad (6)$$

Definition 1. *The set $\Pi \subset \mathbb{R}^n$ is called a Poincaré section or simply a section for (1) if Π is connected manifold of codimension 1 and at every point $x \in \Pi$ vector field f is transversal to Π .*

In practice it is very convenient to define a Poincaré section Π as a subset of zeroes of a smooth scalar function

$$\alpha: \mathbb{R}^n \rightarrow \mathbb{R} \quad (7)$$

for which zero is a regular value. In the sequel we will always assume that a section is given by

$$\Pi = \Pi_{\alpha, C} = \{x : \alpha(x) = 0 \wedge D\alpha(x)(f(x)) \neq 0 \wedge C(x)\}, \quad (8)$$

where C is a predicate that stands for additional constraints on the section (like crossing direction, restriction on the domain, etc.). The transversality condition $D\alpha(x)(f(x)) \neq 0$ means that the flow is not tangent to Π at every $x \in \Pi$. We will often write Π or Π_α instead of $\Pi_{\alpha, C}$ if α and/or C are clear from the context or irrelevant for the reasoning.

Definition 2. *Let Π be a section. We define a map $t_\Pi : \mathbb{R}^n \rightarrow \mathbb{R}$ in the following way*

1. $x \in \text{dom } t_\Pi$ iff there is $t > 0$ such that $\varphi(t, x) \in \Pi$,
2. for $x \in \text{dom } t_\Pi$ we set $t_\Pi(x) = \inf \{t > 0 : \varphi(t, x) \in \Pi\}$.

We will call the function t_Π the flow time to section Π .

Definition 3. *Let Π_1, Π_2 be sections for (1). A Poincaré map $\mathcal{P} : \Pi_1 \rightarrow \Pi_2$ is defined by $\mathcal{P}(x) = \varphi(t_{\Pi_2}(x), x)$ provided $t_{\Pi_2}(x)$ exists. We will denote the restriction of t_{Π_2} to Π_1 by $t_\mathcal{P}$.*

2. The main algorithm

In this section we present the main algorithm for computation of rigorous enclosures of Poincaré maps. Here we assume that Poincaré sections Π_1, Π_2 and associated Poincaré map $\mathcal{P} : \Pi_1 \rightarrow \Pi_2$ are fixed. We also assume that an affine change of coordinates $x \rightarrow A(x - y)$ is given, where A is a linear isomorphism and $y \in \Pi_2$ is a vector.

Our goal is to construct an algorithm that for given $X \subset \Pi_1$ computes as tiny as possible enclosure Y such that

$$A(\mathcal{P}(X) - y) \subset Y. \quad (9)$$

Let us comment briefly on the role of the choice of the above coordinate system, as it crucial in further analysis. The set $\mathcal{P}(X)$ is treated as a subset of \mathbb{R}^n . Although in our algorithm sections can be nonlinear, the algorithm was motivated by the simplest case, when Π_2 is a hyperplane. Assume $y \in \Pi_2$. The matrix A should be chosen as $A = B^{-1}$, where one column (say first) of B is transverse to Π_2 while the remaining columns of B span $T_y \Pi_2$, that is they give a coordinate system $(0, x_2, \dots, x_n) \rightarrow y + B(0, x_2, \dots, x_n)$ on Π_2 . With this choice of A , computation of an enclosure of $\mathcal{P}(X)$ in coordinates $(0, x_2, \dots, x_n)$ is simply projection of the set $\varphi(t_{\Pi_2}(X), X)$ onto all coordinates but the first. The first column of B controls direction of projection of \mathbb{R}^n onto section Π_2 , while proper choice of the basis of $T_y \Pi_2$ helps in reducing wrapping effect on the section.

The algorithm consists of the following two steps. First, given a rough enclosure for the return time $t_{\Pi_2}(X)$ we try to obtain sharp bounds for it — Section 2.2. Then, we compute $\mathcal{P}(X)$ in a given affine coordinate system, that is an enclosure Y for $A(\mathcal{P}(X)-y)$ — Section 2.3. To suppress overestimation in both steps we take advantage from the knowledge about internal representation of subsets of \mathbb{R}^n used by the underlying rigorous ODE solver. Abstract assumptions on these data structures and their sample realisations will be presented in Section 2.1.

2.1. Representation of sets in rigorous ODE solvers

Every rigorous ODE solver uses its own internal representation of subsets of \mathbb{R}^n and solutions to IVP. When a set of initial condition is propagated by a dynamical system and on each step the image is bounded by an interval vector (product of intervals), then typically we observe the wrapping effect that leads to huge overestimation. On the other hand when the image is bounded by some non-linear shape, e.g given by multidimensional polynomials (like in the case of Taylor models [21]), then the result is more accurate but the computational cost increases rapidly with the dimension and the degree of the polynomial.

In [18, 19, 20] the sets are represented (see [24]) as parallelepipeds, doubletons and tripletons. These strategies provide a good compromise between speed and accuracy as shown in [25].

A *doubleton* is a tuple $(x, C, \mathbf{r}_0, Q, \mathbf{q})$, where $x \in \mathbb{R}^n$, $\mathbf{r}_0, \mathbf{q} \subset \mathbb{R}^n$ are interval vectors such that $0 \in \mathbf{r}_0 \cap \mathbf{q}$ and $C, Q \in \mathbb{R}^{n \times n}$ are matrices with Q being invertible and usually close to orthogonal. It represents set of points in \mathbb{R}^n defined by

$$X = \{x + Cr_0 + Qq \mid r_0 \in \mathbf{r}_0, q \in \mathbf{q}\}. \quad (10)$$

A *tripleton* is defined as a tuple $(x, C, \mathbf{r}_0, Q, \mathbf{q}, B, \mathbf{r})$ where $x \in \mathbb{R}^n$, $\mathbf{r}_0, \mathbf{q}, \mathbf{r} \subset \mathbb{R}^n$ are interval vectors containing 0 and $C, Q, B \in \mathbb{R}^{n \times n}$ are matrices. Geometrically it is an intersection of two doubletons, that is

$$X = \{x + Cr_0 + Qq \mid r_0 \in \mathbf{r}_0, q \in \mathbf{q}\} \cap \{x + Cr_0 + Br \mid r_0 \in \mathbf{r}_0, r \in \mathbf{r}\}. \quad (11)$$

The matrix Q is assumed to be close to orthogonal and invertible, while on B we only assume it is invertible.

In the sequel we assume that an abstract data structure called `RepresentableSet` is defined and it represents a subset of \mathbb{R}^n . For example as `RepresentableSet` one can take doubleton or tripleton. We also assume that for given `RepresentableSet` two algorithms `eval` and `affineTransform` are provided. Their expected inputs and outputs are defined by Algorithm 1 and Algorithm 2. For doubleton representation their possible realisations are given by Algorithm 3 and Algorithm 4, respectively.

Algorithm 1: `EVAL`

Input: $X \subset \mathbb{R}^n$: `RepresentableSet`

Input: $g : \mathbb{R}^n \rightarrow \mathbb{R}^m$: smooth function

Output: An enclosure for $g(X)$

Observe, that the assumption $0 \in \mathbf{r}_0 \cap \mathbf{q}$ guarantees that $x \in X$ and thus $[[g](x) + (MC)\mathbf{r}_0 + (MQ)\mathbf{q}]_I$ is an enclosure of $g(x + Cr_0 + Qq)$ in Algorithm 3.

Algorithm 2: AFFINETRANSFORM

Input: $X \subset \mathbb{R}^n$: RepresentableSet

Input: $A : \mathbb{R}^n \rightarrow \mathbb{R}^m$: linear map

Input: $y \in \mathbb{R}^n$

Output: An enclosure of $A(X - y)$

Algorithm 3: EVAL

Input: $x + Cr_0 + Qq \subset \mathbb{R}^n$: Doubleton

Input: $g : \mathbb{R}^n \rightarrow \mathbb{R}^m$: smooth function

Output: An enclosure of $g(x + Cr_0 + Qq)$

$X \leftarrow [x + Cr_0 + Qq]_I$; // enclose set as interval vector

$M \leftarrow [Dg](X)$; // enclose derivative as interval matrix

return $[g](X) \cap [[g](x) + (MC)r_0 + (MQ)q]_I$;

2.2. Refinement of return time $t_\varphi(X)$

Assume that sections $\Pi_1, \Pi_2 \subset \mathbb{R}^n$ are defined as sets of zeroes of smooth functions $\alpha_1, \alpha_2 : \mathbb{R}^n \rightarrow \mathbb{R}$. Computation of a rough enclosure of the return time $t_{\Pi_2}(X)$ for $X \in \Pi_1$ can be realized in the following steps:

1. Find $t_1 > 0$ such that $t_\varphi(X) \geq t_1$. This can be done by checking $\varphi([\delta, t_1], X) \cap \Pi_2 = \emptyset$ where δ is the lower bound for the return time $t_\varphi(X)$ coming from transversality of the flow for both sections.
2. Find $t_2 > t_1$ such that for $x \in X$ there holds $\alpha_2(\varphi(t_2, x))\alpha_2(\varphi(t_1, x)) < 0$. This guarantees that the function α_2 changes the sign on the solution segment $\varphi([t_1, t_2], x)$.
3. Check transversality condition:

$$D\alpha_2(\varphi(t, x))(f(\varphi(t, x))) \neq 0 \text{ for } t \in [t_1, t_2], x \in X. \quad (12)$$

If all steps do not fail then $[t_1, t_2]$ is an upper bound for the return time $t_\varphi(X)$. This rough estimation can be significantly improved by applying Interval Newton Operator [26] to the following univariate function

$$g_x(t) := \alpha_2(\varphi(t, x)). \quad (13)$$

Lemma 4 (Interval Newton Operator). *Let $g : \mathbb{R}^n \rightarrow \mathbb{R}^m$ be a smooth function and let X be a convex, closed set X . For fixed $x_0 \in X$ the interval Newton operator is defined as*

$$N(g, x_0, X) = x_0 - [Dg(X)]_I^{-1} [g](x_0). \quad (14)$$

Algorithm 4: AFFINETRANSFORM

Input: $x + Cr_0 + Qq \subset \mathbb{R}^n$: Doubleton

Input: $A : \mathbb{R}^n \rightarrow \mathbb{R}^m$: linear map

Input: $y \in \mathbb{R}^n$

Output: An enclosure for $A(x + Cr_0 + Qq - y)$

return $[A((x - y) + Cr_0 + Br)]_I \cap [A(x - y) + (AC)r_0 + (AQ)q]_I$;

- If $N(g, x_0, X) \subset \text{int}(X)$ then the g has in X unique zero x_* such that $x_* \in N(g, x_0, X)$.
- If $x \in X$ is a zero of g then $x \in N(g, x_0, X)$.

Algorithm 5: REFINEReturnTime

Input: $[t_1, t_2]$: an interval that encloses $t_{\Pi_2}(X)$
Input: X_1 : RepresentableSet that encloses $\varphi(t_1, X)$
Input: α_2 : function that defines section Π_2
Input: f : underlying vector field
Output: Improved bound for $t_{\Pi_2}(X)$

```

 $t_0 \leftarrow (t_1 + t_2)/2;$ 
 $X_0 \leftarrow \text{RepresentableSet}$  that encloses  $\varphi(t_0 - t_1, X_1);$  // from ODE solver
 $\mathbf{g}_0 \leftarrow \text{eval}(X_0, \alpha_2);$ 
 $\mathbf{e} \leftarrow \text{eval}(X_1, \varphi([0, t_2 - t_1], \cdot));$  // enclosure from ODE solver
 $\mathbf{g} \leftarrow \text{eval}(\mathbf{e}, \nabla\alpha_2(\cdot) \cdot f(\cdot));$ 
return  $[t_1, t_2] \cap (t_0 - \mathbf{g}_0/\mathbf{g});$ 

```

Lemma 5. Assume the Algorithm 5 is called with the correct arguments and returns T . Then $t_{\Pi_2}(X) \subset T \subset [t_1, t_2]$.

Proof: Let us fix $x \in X$. By the assumptions of the Algorithm 5 we have $x_1 := \varphi(t_1, x) \in X_1$. Moreover, since $t_{\Pi_2}(x) \in [t_1, t_2]$ we have $t_{\Pi_2}(x) = t_1 + t_{\Pi_2}(x_1)$. We will apply the Interval Newton Operator [26] to the function g_{x_1} defined by (13) in order to obtain a tighter enclosure for

$$t_{\Pi_2}(x_1) \in [0, t_2 - t_1] \cap g_{x_1}^{-1}(0).$$

The interval Newton operator applied to g_{x_1} reads

$$N(g_{x_1}, t_0 - t_1, [0, t_2 - t_1]) = (t_0 - t_1) - [g_{x_1}](t_0 - t_1) / [g'_{x_1}]([0, t_2 - t_1]).$$

It is easy to see that for $x \in X$ the algorithm encloses the following quantities with $t_0 = (t_1 + t_2)/2$ and $t \in [0, t_2 - t_1]$

$$\begin{aligned} g_{x_1}(t_0 - t_1) &= \alpha_2(\varphi(t_0 - t_1, x_1)) \in \mathbf{g}_0, \\ g'_{x_1}(t) &= \nabla\alpha_2(\varphi(t, x_1)) \cdot f(\varphi(t, x_1)) \in \mathbf{g}. \end{aligned}$$

Therefore $t_{\Pi_2}(x_1) \in (t_0 - t_1) - \mathbf{g}_0/\mathbf{g}$ and in consequence

$$t_{\Pi_2}(x) = t_1 + t_{\Pi_2}(x_1) \in t_0 - \mathbf{g}_0/\mathbf{g},$$

which completes the proof. \square

Observe that \mathbf{g} does not contain zero because the transversality condition (12) is satisfied on $[t_1, t_2]$. Algorithm 5 can be iterated until no improvement is observed. In most cases it stabilizes after 2 – 3 iterations provided $[t_1, t_2]$ was already a good initial bound for $t_{\varphi}(X)$. Observe that $\text{diam}(t_{\varphi}(X))$ is proportional to $\text{diam}(\alpha_2(X_0))$, which is up to a constant the size of X_1 in the "direction" of the section.

Remark 6. *It is very important to use information about representation of the set X_0 in computation $\mathbf{g}_0 \leftarrow \text{eval}(X_0, \alpha_2)$. For example, for $\alpha_2(x, y) = x - y$ and the set $X_0 = x + Cr = \begin{bmatrix} 1 + \varepsilon \\ 1 \end{bmatrix} + \begin{bmatrix} 1 & 1 \\ 1 & -1 \end{bmatrix} \begin{bmatrix} [-1, 1] \\ 0 \end{bmatrix}$ a direct evaluation in interval arithmetics gives*

$$\alpha_2(X_0) \subset \alpha_2((1 + \varepsilon, 1) + ([-1, 1], [-1, 1])) = \alpha_2(([\varepsilon, 2 + \varepsilon], [0, 2]) = [-2 + \varepsilon, 2 + \varepsilon].$$

The diameter of obtained estimate is 4 and as it contains 0 we cannot conclude if the set X_0 is before or after the section. Representing X_0 as doubleton $(x, C, \mathbf{r}_0, Q = Id, \mathbf{q} = 0)$ and applying Algorithm 3 gives

$$\alpha_2(X_0) \subset [\alpha_2](1 + \varepsilon, 1) + \left(\nabla \alpha_2(X_0)^T \begin{bmatrix} 1 & 1 \\ 1 & -1 \end{bmatrix} \right) \begin{bmatrix} [-1, 1] \\ 0 \end{bmatrix} = [\varepsilon, \varepsilon] + \begin{bmatrix} 0 & 2 \\ 0 & 0 \end{bmatrix} \begin{bmatrix} [-1, 1] \\ 0 \end{bmatrix} = [\varepsilon, \varepsilon].$$

This sharp bound, even for ε close to zero, allows to verify relative location of the set X_0 and the section.

2.3. Computation of Poincaré map

In this section we present Algorithm 6, which realizes the last step of computation of an enclosure of $A(\mathcal{P}(x) - y)$ for $x \in X$, where $y \in \Pi_2$ and A is a linear mapping. That is, we represent $\mathcal{P}(x)$ in a local affine coordinate system near y . Let us emphasize, that the restriction to affine coordinates is reasonable keeping in mind that the underlying ODE solver represents subsets of \mathbb{R}^n usually as doubletons or tripletons.

Algorithm 6: COMPUTEPOINCARÉMAP

Input: $[t_1, t_2]$: an interval that encloses $t_{\mathcal{P}}(X)$
Input: X_1 : RepresentableSet that encloses $\varphi(t_1, X)$
Input: f : underlying vector field
Input: y : a vector
Input: A : a linear map
Output: An enclosure of $A(\mathcal{P}(X) - y)$

```

 $e \leftarrow \text{eval}(X_1, \varphi([0, t_2 - t_1], \cdot));$  // enclosure from ODE solver
 $t_0 \leftarrow (t_1 + t_2)/2;$ 
 $\Delta t \leftarrow [t_1, t_2] - t_0;$ 
 $X_0 \leftarrow \text{RepresentableSet}$  that encloses  $\varphi(t_0 - t_1, X_1);$  // call to ODE solver
 $\mathbf{y}_0 \leftarrow \text{affineTransform}(X_0, A, y);$ 
 $\mathbf{y} \leftarrow \text{eval}(X_0, A \circ f) \cdot \Delta t;$ 
 $\Delta \mathbf{y} \leftarrow \frac{1}{2} A \cdot [Df](\mathbf{e}) \cdot [f](\mathbf{e}) \cdot \Delta t^2;$ 
 $\mathbf{z} \leftarrow (\mathbf{y}_0 + \mathbf{y} + \Delta \mathbf{y}) \cap [A(\mathbf{e} - y)]_J;$ 
return  $\mathbf{z};$ 

```

Before we state and prove properties of Algorithm 6, let us comment again (see the paragraph after (9)) on the role of the coordinate system

$$x \mapsto z = A(x - y),$$

as it crucial in further analysis. First, let us observe that the set $\mathcal{P}(X) \subset \Pi_2 \subset \mathbb{R}^n$ is treated as a subset of full phase space. Formally the algorithm computes an enclosure for $\mathbf{z} = A(\mathcal{P}(X) - y) \subset$

\mathbb{R}^n but what we usually are interested in is indeed $\mathcal{P}(X)$. We will show, that the proper choice of the matrix A helps to extract from computed result $A(\mathcal{P}(X) - y)$ much tighter enclosure on $\mathcal{P}(X)$ than from a naive algorithm, that is $\mathcal{P}(X) \subset \text{eval}(X_1, \varphi([0, t_2 - t_1], \cdot))$.

If the Poincaré section Π_2 is a hyperplane with $y \in \Pi_2$ then the matrix A should be chosen as $A = B^{-1}$, where one column (say first) of B is transverse to Π_2 and it defines direction of projection of \mathbb{R}^n onto Π_2 , while the remaining columns of B should span $T_y\Pi_2$. Denote by $z \supset A(\mathcal{P}(X) - y)$ the result of Algorithm 6. With this choice of A we have

$$\mathcal{P}(X) \subset y + B(0, z_2, \dots, z_n)^T$$

because all but first columns of B span the section $T_y\Pi_2$. What we get is an enclosure of $\mathcal{P}(X)$ in the form of an affine set.

Lemma 7. *Assume the Algorithm 6 is called with its arguments, where f is of class C^1 . Let z be computed result. Then $A(\mathcal{P}(X) - y) \subset z$.*

Proof: First observe that the computed quantity e is an enclosure of $\mathcal{P}(X)$ and therefore $A(\mathcal{P}(X) - y) \subset A(e - y)$. We have to show that $A(\mathcal{P}(X) - y) \subset y_0 + y + \Delta y$.

Denote by $T = [0, t_2 - t_1]$. The flow φ is C^2 with respect to time variable. Using the Taylor theorem with the Lagrange remainder we obtain

$$\mathcal{P}(X) \subset \varphi(T, X_1) = \varphi(\Delta t, X_0) \subset X_0 + f(X_0)\Delta t + \frac{1}{2}Df(e)f(e)\Delta t^2,$$

where $X_0, e, \Delta t$ are defined as in Algorithm 6. Therefore

$$\begin{aligned} A(\mathcal{P}(X) - y) &\subset A(X_0 - y) + Af(X_0)\Delta t + \frac{1}{2}ADf(e)f(e)\Delta t^2 \\ &\subset y_0 + y + \Delta y. \end{aligned}$$

□

Remark 8. *It is extremely important to compute y_0 and y taking into account the representation of X_0 (Algorithms `eval` and `affineTransform`) in order to reduce wrapping effect in evaluation of products $A \cdot X_0$ and $A \cdot f(X_0)$. These terms are the most important components of the result. The quantity Δy is expected to be small in comparison to y_0 . Indeed, if the diameter of the set is small, then we expect that the diameter of crossing time $[t_1, t_2]$, and so Δt is proportional to diameter of the set X_0 and thus $\Delta y \in O(\text{diam}(X_0)^2)$. More precisely Δt is proportional to diameter of the set X_0 in the direction of the flow.*

In the next section we will argue, that playing with the choice of Poincaré section and coordinate system A on it we can make the term y also small in comparison to $\text{diam}(y_0)$.

3. Varying Poincaré section and coordinates on it.

Definition 9. *Assume p is a periodic point of (1) of period T . $\lambda \in \mathbb{C}$ is a Floquet multiplier for the periodic orbit through p if it is an eigenvalue of $D_x\varphi(T, p)$.*

It is well known that the set of Floquet multipliers depends on the orbit, only, i.e. is the same for all choices of p on the periodic orbit. Moreover, the set of Floquet multipliers always contains $\lambda = 1$ corresponding to the orbit direction $f(p)$ and the eigenvalues for the Poincaré map on any transversal to $f(p)$ section containing p give all Floquet multipliers different from 1.

In the remainder of the section we will often say that a “vector $f(p)$ is orthogonal to the section Π ”. In saying that, we silently assumed that we have a scalar product given by $\langle x | y \rangle = \sum_i x_i y_i$. Stated as such the notion of “orthogonality” depends on the coordinate frame used. The “orthogonality” in the above sense is used as a measure to assure that the vector field is far from being tangent to the section Π .

As mentioned in Section 2.3, the term y_0 is the main component of the result returned by Algorithm 6 and computation of y_0 takes into account representation of the sets by an underlying ODE solver (algorithm `affineTransform`). In this section we will give some heuristics on how one can reduce diameter of the component y . Our considerations will be supported by the following case studies

- the Michelson system [27] — a 3D system given by

$$x' = y, \quad y' = z, \quad z' = c^2 - y - \frac{1}{2}x^2 \quad (15)$$

around an approximate periodic orbit

$$u_M \approx (0, 1.32825866108569290258, 0) \quad (16)$$

for parameter $c = 0.8$. It has been shown [5] that for a wide range of parameter values including $c = 0.8$ certain Poincaré map of this system is Σ_4 chaotic and hyperbolic periodic orbit u_M is part of chaotic invariant set. Approximate Floquet multipliers of u_M are 1 and

$$\lambda_{M_1} \approx -21.57189303583905, \quad \lambda_{M_2} \approx -0.046356617768258279 \quad (17)$$

- the Falkner-Skan equation [28] — a 3D system given by

$$x' = y, \quad y' = z, \quad z' = c(y^2 - 1) - xz \quad (18)$$

around an approximate periodic orbit

$$u_{FS} \approx (0, 0.939712208779672476275, 0) \quad (19)$$

for parameter $c = 250$. As shown in [29], this periodic orbit belongs to a family parameterized by $c \in [\frac{9}{8}, 100000]$. The choice of $c = 250$ is motivated by the fact, that this orbit appears to be ill-conditioned for the method of minimization of the crossing time $[t_1, t_2]$ — see Section 3.4. It is hyperbolic with approximate Floquet multipliers 1 and

$$\lambda_{FS_1} \approx -3.1255162015308575, \quad \lambda_{FS_2} \approx -0.31994714969329141. \quad (20)$$

Moreover, the system is stiff near the initial condition, which may cause additional problems for an ODE solver.

- the Rössler system [30] – a 4D system given by

$$x' = -y - w, \quad y' = x + ay + z, \quad z' = dy + cw, \quad w' = xw + b \quad (21)$$

around an approximate periodic orbit

$$u_{R_h} \approx (-29.841563300389689, 0, 15.047757539453583, 0.10059818458161384) \quad (22)$$

for parameter values $a = 0.25$, $b = 3$, $c = -0.5$, $d = 0.05$. As shown in [6], this system is hyperchaotic (two positive Lyapunov exponents) and u_{R_h} belongs to hyperchaotic invariant set. Approximate Floquet multipliers are 1 and

$$\lambda_{R_{h1}} \approx -2.9753618617897111, \quad \lambda_{R_{h2}} \approx 1.11933293616997, \quad \lambda_{R_{h3}} \approx -2 \cdot 10^{-18} \quad (23)$$

- the Rössler system (21) around an approximate periodic orbit

$$u_{R_{pd}} \approx (-16.051468914417546, 0, 8.362179513564907, 0.18738588995067224) \quad (24)$$

for parameter values $a = 0.25$, $b = 3$, $c = -0.397617541005413$, $d = 0.05$. This orbit belongs to the same family as u_{R_h} parameterized by c . Near this particular parameter value the family undergoes the period doubling bifurcation. The Floquet multipliers are 1 and

$$\lambda_{R_{pd1}} \approx 1.2039286263296654, \quad \lambda_{R_{pd2}} \approx -1, \quad \lambda_{R_{pd3}} \approx -6 \cdot 10^{-17} \quad (25)$$

and absolute values of $\lambda_{R_{pd1}}$ and $\lambda_{R_{pd2}}$ are close or very close to one, hence non-linear terms can play significant role near this orbit. We expect that this orbit may be difficult for both ODE solver and our algorithm for computation of Poincaré map, because the ODE solver uses affine representation of sets and also the Algorithm 6 computes an enclosure of \mathcal{P} in affine form.

Shapes of these four periodic orbits are shown in Figure 1.

3.1. Reduction of sliding and wrapping effects

In this paragraph we assume that we do not have freedom in choosing the Poincaré section. This is common in hybrid systems (sections are guards between regions with different vector fields) or when one wants to take advantage of some specific properties of a system, like symmetries.

Recall, that \mathbf{y}_0 is the main component of the result returned by Algorithm 6. In what follows we will argue that the diameter of the projection of \mathbf{y} onto section can be reduced by a proper choice of direction of projection, which is hidden in the coordinate system A .

Theorem 10. *Assume the Algorithm 6 is called with its arguments $y \in X_0 \cap \Pi$ and the matrix $A = B^{-1}$, where*

$$B = \left[\begin{array}{c|c} f(y) & M \end{array} \right]$$

and columns in M span $T_y\Pi$. Then

$$\mathbf{y} + \Delta\mathbf{y} \in (\Delta\mathbf{t}, 0, 0, \dots) + O(\text{diam}(X_0)^2).$$

Proof: In Algorithm 6, the quantity \mathbf{y} is computed as $\mathbf{y} \leftarrow \text{eval}(X_0, A \circ f) \cdot \Delta\mathbf{t}$ which is realized by the intersection of direct evaluation in interval arithmetic and application of the mean value theorem to $A \circ f$. Thus

$$\mathbf{y} \subset [Af(x_0) + A[Df](X_0)\Delta X_0]_I \Delta\mathbf{t},$$

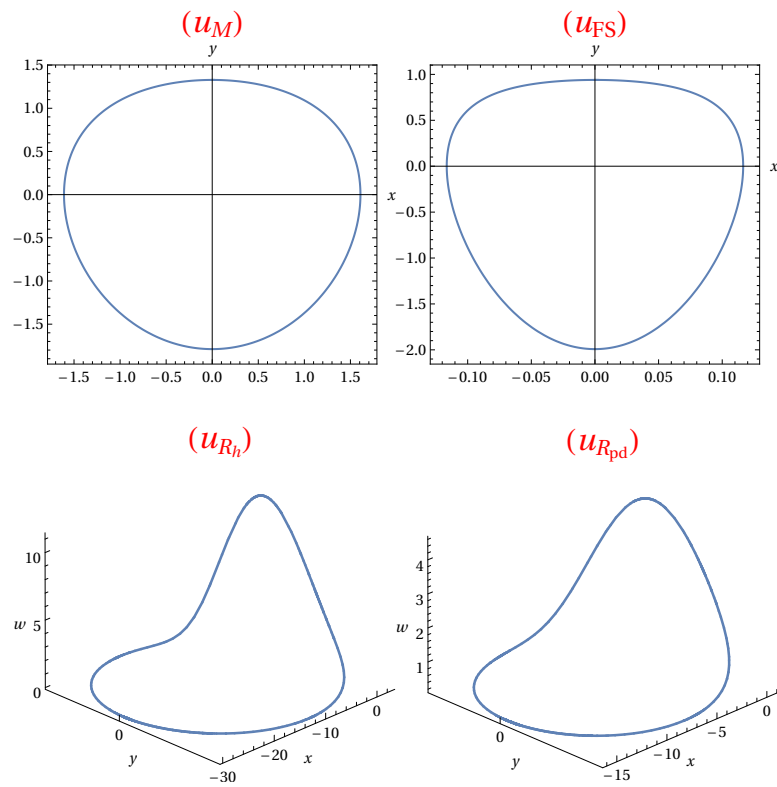


Figure 1: The four periodic orbits u_M , u_{FS} , u_{R_h} and $u_{R_{pd}}$, for the Michelson system [27], Falkner-Skan system [28] and the Rössler system [30], respectively.

where $x_0 = \text{mid}(X_0)$ and $\Delta X_0 = X_0 - x_0$. We have

$$A[Df](X_0)\Delta X_0\Delta t \in O(\text{diam}(X_0)^2) \quad (26)$$

because $\text{diam}(\Delta t) \in O(\text{diam}(X_0))$. Since $y \in X_0$, which is a convex set, we have

$$Af(x_0)\Delta t \in (Af(y))\Delta t + [ADf(X_0)]_I(x_0 - y)\Delta t.$$

By the assumptions on A , we have $Af(y) = (1, 0, 0, \dots)$ and thus

$$[(Af(y))\Delta t]_I = (\Delta t, 0, 0, \dots). \quad (27)$$

We also have

$$[ADf(X_0)]_I(x_0 - y)\Delta t \in O(\text{diam}(\Delta X_0)\text{diam}(\Delta t)) = O(\text{diam}(\Delta X_0)^2). \quad (28)$$

Gathering (26)–(28) we get $y = (\Delta t, 0, 0, \dots) + O(\text{diam}(X_0)^2)$. The component Δy contains the factor Δt^2 and thus its diameter is also quadratic in diameter of X_0 . \square

Remark 11. *In the proof of Theorem 10 we assumed that evaluations $f(x_0)$ and $f(y)$ are exact and thus of diameter zero.*

Corollary 12. *Assume that the section Π is a hyperplane. Denote by $z = y + y_0 + \Delta y = (z_1, \dots, z_n)$ result of Algorithm 6. Under assumptions of Theorem 10 and*

$$\mathcal{P}(X) \subset y + B(0, z_2, \dots, z_n)^T.$$

Moreover,

$$\mathcal{P}(X) \subset y + B(0, y_2, \dots, y_n)^T + O(\text{diam}(X_0)^2).$$

Proof: Since $y \in \Pi$ and all but first columns of B span $T_y\Pi$, we have that

$$\Pi = \left\{ y + B(0, z_2, \dots, z_n)^T : z_2, \dots, z_n \in \mathbb{R} \right\}.$$

Therefore,

$$\mathcal{P}(X) \subset (y + Bz) \cap \Pi = y + B(0, z_2, \dots, z_n)^T.$$

From Theorem 10 we have that

$$(0, z_2, \dots, z_n) = (0, y_2, \dots, y_n) + O(\text{diam}(X_0)^2),$$

which completes the proof of the second assertion. \square

3.2. Choosing coordinate system on Poincaré section close to fixed point

Let $u \in \Pi$ be an approximation of a fixed point of Poincaré Map $\mathcal{P} : \Pi \rightarrow \Pi$ and assume Π is an affine section

$$\Pi = \left\{ u + \sum_{i=2}^n z_i v_i \mid z_i \in \mathbb{R} \right\},$$

where $\{v_2, \dots, v_n\}$ are linearly independent. We introduce here our two strategies for setting up coordinate system centred at u . In the first step we compute non-rigorously $D\mathcal{P}(u)$ in the coordinate system

$$(z_2, \dots, z_n) = u + \sum_{i=2}^n z_i v_i.$$

Let $M \in \mathbb{R}^{(n-1) \times (n-1)}$ be a square matrix with columns corresponding to normalized eigenvectors of $D\mathcal{P}(u)$. In the second step we choose any vector v_1 linearly independent with $\{v_2, \dots, v_n\}$ and define matrices

$$V = [v_1 \ v_2 \ \dots \ v_n], \quad Q = \begin{bmatrix} 1 & 0 \\ 0 & M \end{bmatrix} \quad \text{and} \quad B = VQ. \quad (29)$$

Depending on the choice of v_1 we call this strategy:

- **diag+normal** if v_1 is orthogonal to the section Π ,
- **diag+flowdir** if v_1 is normalized vector field at u i.e. $v_1 = \frac{f(u)}{\|f(u)\|}$.

3.3. Choosing coordinate systems on Poincaré section — experiments.

In this section we present results of numerical experiments regarding various strategies of choosing the matrix A in Algorithm 6. All results strongly confirm theoretical findings of Theorem 10. In our test suite, we have chosen “standard” sections, that is $x = 0$ for orbits u_M and u_{FS} and $y = 0$ for u_{R_h} and $u_{R_{pd}}$ — see (16), (19), (22) and (24). We also reorder coordinates in the Rössler system (21) as (y, x, z, w) so that in each case the section is defined by vanishing first coordinate.

With some abuse on notation, by the same letter \mathcal{P} we will denote Poincaré map for each of these systems and by u corresponding periodic orbit for this system. In each case u is a fixed point of \mathcal{P}^2 (the orbit crosses section Π twice in opposite directions). Let matrix B be defined as in (29).

Our aim is to compute $z = B^{-1}(\mathcal{P}^2(X) - u)$, where $X = u + Br$, $r = \frac{1}{2}s \cdot (0, [-1, 1], \dots, [-1, 1])$ and $s > 0$ is the diameter of the set X in the coordinate system B . Observe, that set X does not depend on the choice of vector v_1 used to define V and B .

We compare three choices of matrix $A = B^{-1}$ and vector y in Algorithm 6:

- **cartesian** — in this approach we compute Poincaré map in the coordinate system of the ODE by running Algorithm 6 with arguments $A = \text{Id}$, $y = 0$ and then we change coordinates evaluating $z = B^{-1}(\mathcal{P}^2(X) - u)$,
- **diag+normal** — we run Algorithm 6 with its arguments $A = B^{-1}$, $y = u$, where v_1 orthogonal to the section,
- **diag+flowdir** — we run Algorithm 6 with its arguments $A = B^{-1}$, $y = u$, where $v_1 = \frac{f(u)}{\|f(u)\|}$.

In all computation we have used a rigorous integrator from the CAPD library [19, 18]. Since our goal is to check the properties of the algorithm that computes intersection of set of trajectories with section, we would like to reduce as much as possible the influence of rigorous integration along periodic trajectory. Therefore, we used the Hermite-Obreshkov method [31] of rather high order 50 and high precision interval arithmetics with 200 bits of mantissa [32]. In each case the

initial condition was an affine set $X = u + Br$, as described above, and represented as Tripleton initialized with $X = (u, B, r, \text{Id}, \mathbf{0}, \text{Id}, \mathbf{0})$.

Results of experiments are partially listed in Tables 3, 4, 5 and 6 (columns diag+normal and diag+flowdir) and visualised in Figure 2. These data strongly confirm that **diag+flowdir** strategy (that is Theorem 10) gives the best results. We also observe, that for small and moderate diameters of X , diameter of each component of the result is comparable to what is expected from linearization, that is scaling by corresponding eigenvalue — see column diag+flowdir in Tables 3, 4, 5 and 6. This comment is not valid for the smallest in absolute value eigenvalue for the Rössler system, which is very close to zero and thus rounding errors and truncation errors of underlying ODE integrator are of comparable size.

3.4. Poincaré section near periodic trajectories

In many applications we are free to choose Poincaré sections. Despite Theorem 10, which aims on reducing sliding effect on the section, we can try to minimize crossing time Δt by a proper choice of the section. This should additionally reduce errors coming from components y and Δy in Algorithm 6.

Theorem 13. *Let f be a vector field and denote by φ induced local flow on \mathbb{R}^n . Assume $\varphi(T, x_0) = x_0$ for some minimal $T > 0$ and assume that $\lambda = 1$ is an eigenvalue of $M := D_x \varphi(T, x_0)$ of multiplicity one.*

Let $\Pi = \{x \in \mathbb{R}^n : \alpha(x) = 0\}$ be a local Poincaré section, where $\alpha : \mathbb{R}^n \rightarrow \mathbb{R}$ is smooth, 0 is a regular value of α and $x_0 \in \Pi$. Then

$$(\ker Dt_{\Pi} = T_{x_0} \Pi) \iff (D\alpha(x_0) \text{ is a left eigenvector of } M \text{ for } \lambda = 1).$$

In such case, $t_{\Pi}(x) = t_{\Pi}(x_0) + O(\|x - x_0\|^2)$ for $x \in \Pi$.

Proof: First we let us gather several easy facts which will be used in the proof. Observe that the fact that α is a local section we have

$$\langle D\alpha(x_0) | f(x_0) \rangle \neq 0, \quad (30)$$

$$\ker D\alpha(x_0) = T_{x_0} \Pi. \quad (31)$$

Differentiating the identity $\alpha(\varphi(t_{\Pi}(x), x)) \equiv 0$ at $x = x_0$ we obtain

$$\langle D\alpha(x_0) | f(x_0) \rangle Dt_{\Pi}(x_0) + D\alpha(x_0)M \equiv 0. \quad (32)$$

It is well known that

$$Mf(x_0) = f(x_0), \quad (33)$$

i.e. $f(x_0)$ in an eigenvector for M for $\lambda = 1$. From this and (30,32) we obtain

$$\langle Dt_{\Pi}(x_0) | f(x_0) \rangle = -\langle D\alpha(x_0) | f(x_0) \rangle^{-1} \langle D\alpha(x_0) | f(x_0) \rangle \neq 0. \quad (34)$$

Now we are ready for the proof of our equivalence.

For the proof in \Leftarrow direction, assume that $D\alpha(x_0)$ is a left eigenvector of M for the eigenvalue $\lambda = 1$. From (32) we obtain

$$0 = \langle D\alpha(x_0) | f(x_0) \rangle Dt_{\Pi}(x_0) + D\alpha(x_0)M = \langle D\alpha(x_0) | f(x_0) \rangle Dt_{\Pi}(x_0) + D\alpha(x_0).$$

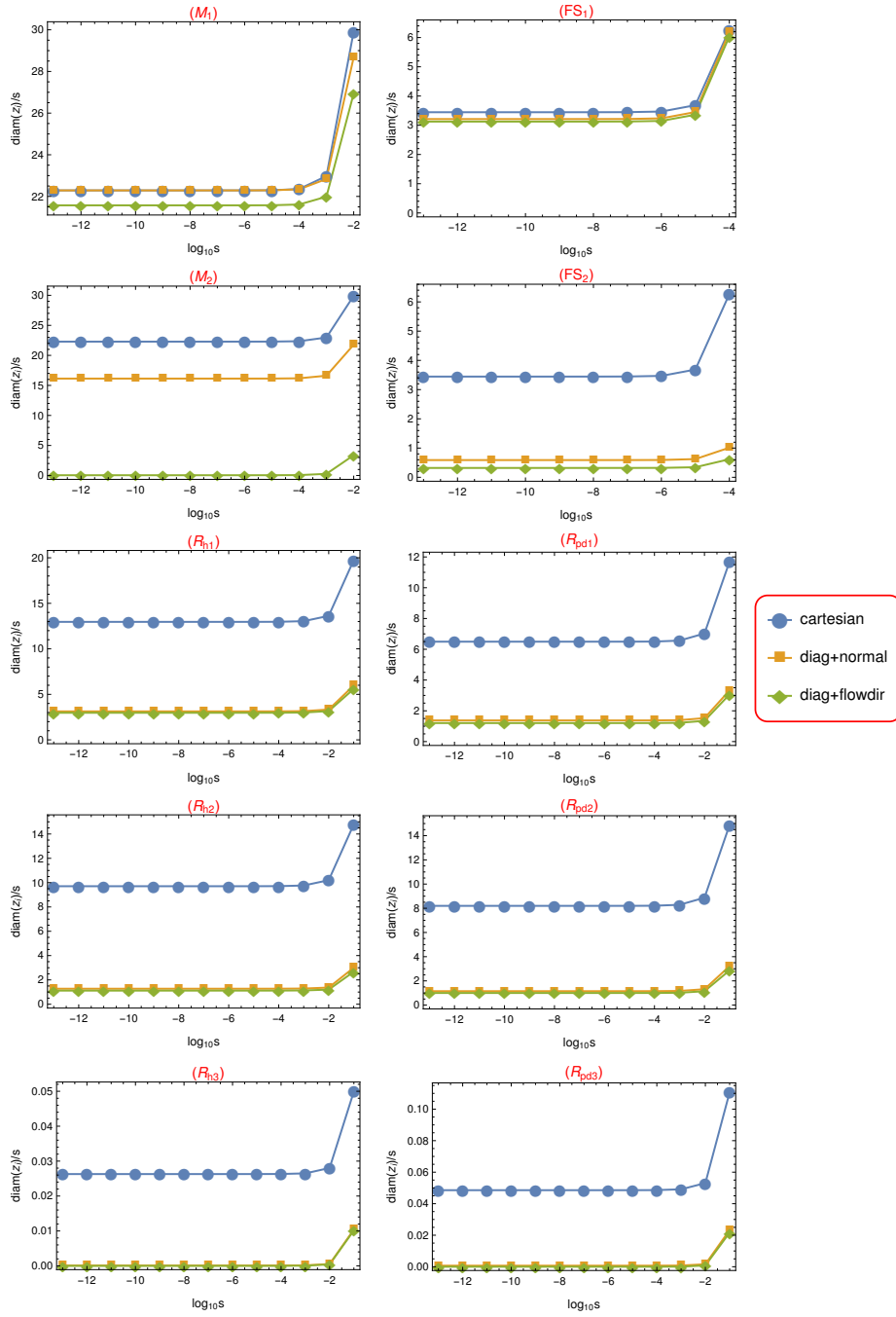


Figure 2: Comparison of enclosures of $z = B^{-1}(\mathcal{P}^2(u + B \cdot r) - u)$ computed by different methods. Horizontal axis corresponds to logarithms of size s of the initial set r . On vertical axis we plot the ratio $\text{diam}(z_i)/s$, which for small s should be close to the corresponding eigenvalue of $D\mathcal{P}^2(u)$. The labels M , FS and R_h and R_{pd} stand for the orbits u_M , u_{FS} , u_{R_h} and $u_{R_{pd}}$, respectively. Additional index indicates coefficient of the result.

This implies that 1-forms $D\alpha(x_0)$ and Dt_Π are proportional and from (30) both are non-zero. Hence from (31) we obtain

$$\ker Dt_\Pi(x_0) = \ker D\alpha(x_0) = T_{x_0}\Pi.$$

For the proof in \Rightarrow direction assume that $\ker Dt_\Pi(x_0) = T_{x_0}\Pi$. From this and (30,31,34) it follows that the forms $D\alpha(x_0)$ and $Dt_\Pi(x_0)$ are non-zero and proportional. Hence from (32) we see that $D\alpha(x_0)$ is a left eigenvector of M for some eigenvalue λ . We will show that $\lambda = 1$.

We have

$$\lambda D\alpha(x_0) = D\alpha(x_0)M,$$

We evaluate both sides of the above equality in $f(x_0)$ and from (33) we obtain

$$\lambda \langle D\alpha(x_0) | f(x_0) \rangle = \langle D\alpha(x_0)M | f(x_0) \rangle = \langle D\alpha(x_0) | Mf(x_0) \rangle = \langle D\alpha(x_0) | f(x_0) \rangle$$

Now from (30) we infer that $\lambda = 1$. This finishes the proof. \square

In what follows, by CTO we will mean a *crossing-time optimal* section chosen according to Theorem 13.

Example: In order to show Theorem 13 in action let us consider the van der Pol equation

$$x' = y, \quad y' = 0.2y(1 - x^2) - x. \quad (35)$$

It is well known that the system has an attracting periodic point. A very accurate approximate initial condition for such periodic point is $u_0 := (x_0, y_0) = (2.0004136789920905, 0.0)$

In the experiment, we will compute bounds on $t_\mathcal{P}(\mathbf{u})$ and $\mathcal{P}(\mathbf{u})$, where $\mathbf{u} = u_0 + \Delta\mathbf{u}$, for various sizes of the set $\Delta\mathbf{u}$ and for two different choices of the Poincaré section.

First, define $\Pi = \{(x, y) \in \mathbb{R}^2 : y = 0\}$. This section is orthogonal to the vector field near the periodic point. In Figure 3 (left panel) we have shown segments of trajectories of the same time-length for various initial conditions of the form $(x_0 + \delta, y_0)$. It is a clear indication, that the return time as a function of δ is monotone near $\delta = 0$. In Table 1 we give data from rigorous computation of Poincaré map obtained from Algorithm 6 with coordinate system $A = \text{Id}$ and $y = u_0$. We see that diameter of the result $\mathcal{P}(\mathbf{u})$ and of the crossing time grow almost linearly with the size of $\Delta\mathbf{u} = [-\delta, \delta], 0$.

In Figure 3 (right panel) we plot trajectory segments of the same time-length of several points at the CTO section near u_0 . This is a numerical evidence, that the return time has a local maximum at periodic point. In Table 2 we give data from rigorous computation of Poincaré map obtained from Algorithm 6 with a coordinate system (x_1, x_2) centred at u_0 and given by normalized vector field at u_0 , that is $(0, -1)$ and the vector spanning the section $(-0.894 \dots, 0.449 \dots)$. As an initial condition for the Algorithm 6 we choose sets of the form $\mathbf{u} = u_0 + (0, [-\delta, \delta]x_2)$. We see that x_2 component grows linearly with δ , as expected. Starting from $\delta = 10^{-7}$ we see that diameter of return time is a flat function (quadratic growth) of δ . For $\delta \leq 10^{-8}$ these values balance near $3.46 \cdot 10^{-14}$ which is close to the machine epsilon in double precision.

Remark 14. *Theorem 13 shows that using CTO section combined with Theorem 10 near a periodic point we can reduce diameters of \mathbf{y} and $\Delta\mathbf{y}$ to $\text{diam}(\mathbf{y}) \in O(\text{diam}(X_0)^3)$ and $\text{diam}(\Delta\mathbf{y}) \in O(\text{diam}(X_0)^4)$, because $\Delta\mathbf{t} \in O(\text{diam}(X_0)^2)$.*

Remark 15. *The CTO section may increase errors coming from sliding effect. In Figure 4 we plot the cosine of the angle between vector field at $u(t)$ and the normal vector to CTO section at $u(t)$ along orbits u_M, u_{FS}, u_{R_h} and $u_{R_{pd}}$. We see that along entire trajectory of u_{FS} the CTO section is almost tangent to the vector field.*

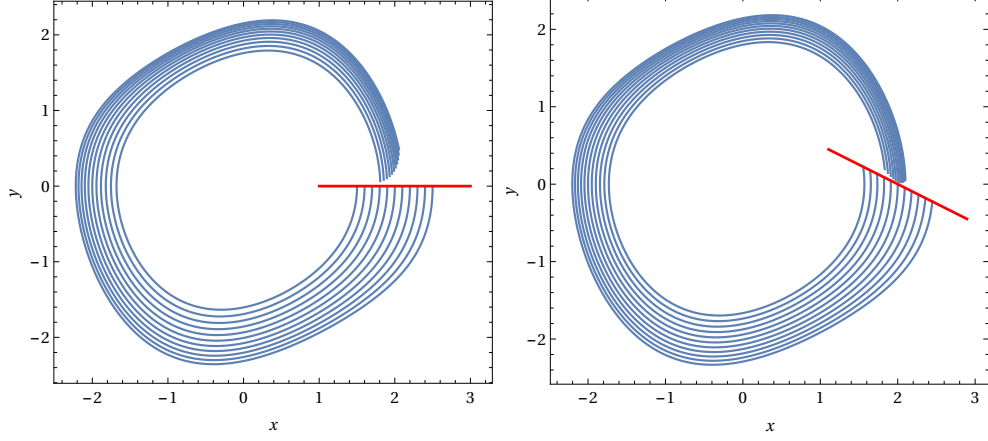


Figure 3: Trajectory segments over the same time range of several points near an attracting periodic point for (35). Left: the Poincaré section is orthogonal to the flow at every point from the section. Right: Poincaré section chosen according to Theorem 13, that is minimizing diameter of the crossing time. Here the return time has a local maximum at periodic point.

$\delta = \frac{1}{2} \text{diam}(\mathbf{u})$	diameter of crossing time	$\pi_x \mathcal{P}(\mathbf{u}) - x_0$
10^{-9}	$3.6 \cdot 10^{-10}$	$[-2.83, 2.83] \cdot 10^{-10}$
10^{-8}	$3.6 \cdot 10^{-9}$	$[-2.83, 2.83] \cdot 10^{-9}$
10^{-7}	$3.6 \cdot 10^{-8}$	$[-2.83, 2.83] \cdot 10^{-8}$
10^{-6}	$3.6 \cdot 10^{-7}$	$[-2.83, 2.83] \cdot 10^{-7}$
10^{-5}	$3.6 \cdot 10^{-6}$	$[-2.83, 2.83] \cdot 10^{-6}$
10^{-4}	$3.61 \cdot 10^{-5}$	$[-2.83, 2.83] \cdot 10^{-5}$
10^{-3}	$3.64 \cdot 10^{-4}$	$[-2.84, 2.84] \cdot 10^{-4}$
10^{-2}	$3.97 \cdot 10^{-3}$	$[-2.93, 2.93] \cdot 10^{-3}$
10^{-1}	$1.18 \cdot 10^{-1}$	$[-6.5, 6.12] \cdot 10^{-2}$

Table 1: Computed diameter of crossing time and an enclosure of Poincaré map for the section $\Pi = \{(x, y) : y = 0\}$ for (35) expressed in the cartesian coordinates.

$\delta = \frac{1}{2} \text{diam}(\mathbf{u})$	diameter of crossing time	$\pi_{x_2} \mathcal{P}(\mathbf{u})$
10^{-9}	$3.46 \cdot 10^{-14}$	$[-2.83, 2.83] \cdot 10^{-10}$
10^{-8}	$3.46 \cdot 10^{-14}$	$[-2.83, 2.83] \cdot 10^{-9}$
10^{-7}	$6.39 \cdot 10^{-14}$	$[-2.83, 2.83] \cdot 10^{-8}$
10^{-6}	$2.99 \cdot 10^{-12}$	$[-2.83, 2.83] \cdot 10^{-7}$
10^{-5}	$2.96 \cdot 10^{-10}$	$[-2.83, 2.83] \cdot 10^{-6}$
10^{-4}	$2.96 \cdot 10^{-8}$	$[-2.83, 2.83] \cdot 10^{-5}$
10^{-3}	$2.97 \cdot 10^{-6}$	$[-2.83, 2.83] \cdot 10^{-4}$
10^{-2}	$3.11 \cdot 10^{-4}$	$[-2.89, 2.89] \cdot 10^{-3}$
10^{-1}	$6.26 \cdot 10^{-2}$	$[-4.66, 4.78] \cdot 10^{-2}$

Table 2: Computed diameter of crossing time and an enclosure of Poincaré map for (35) for a CTO section expressed in (x_1, x_2) coordinates.

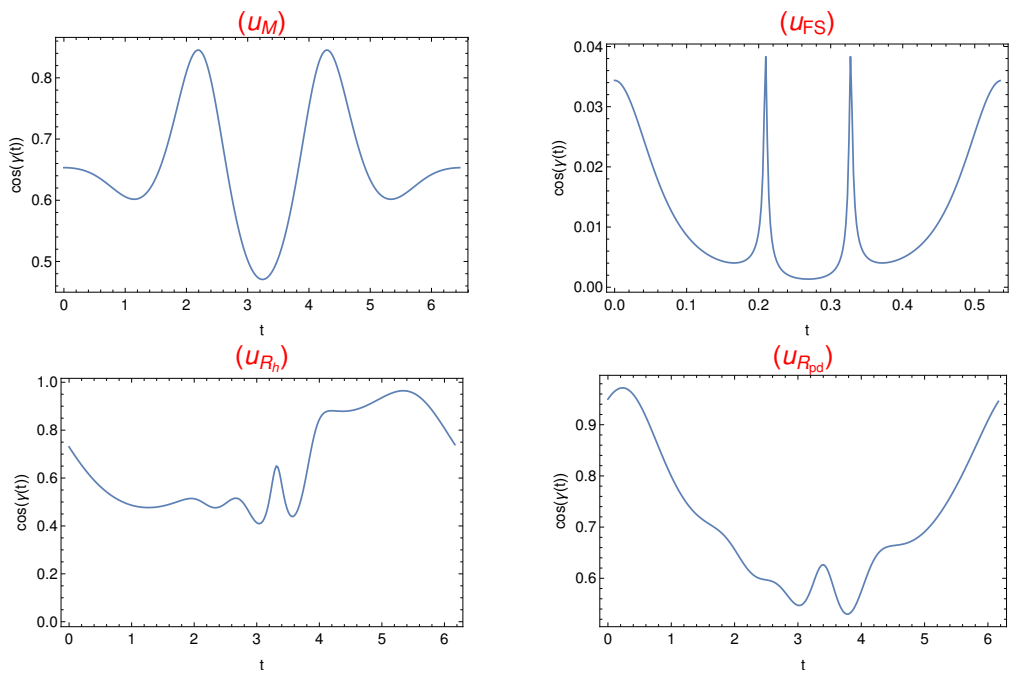


Figure 4: Plot of $\cos(\gamma(t))$, where $\gamma(t)$ is the angle between vector field at $u(t)$ and normal vector to CTO section at $u(t)$ along periodic orbits u_M , u_{FS} , u_{Rh} and u_{Rpd} , respectively. The plot (u_{FS}) shows that the vector field is nearly tangent to the CTO section along entire trajectory.

3.5. Varying Poincaré section — experiments.

In this section we present results of the following experiment. We compare enclosures on Poincaré map for three choices of section for each periodic orbit u_M , u_{FS} , u_{R_h} and $u_{R_{pd}}$, denoted below as u .

- **orthogonal** — the section is chosen as orthogonal to the vector field at u ,
- **CTO** — the section is chosen according to Theorem 13 at u ,
- **max angle CTO** — the section is chosen as CTO but at a point $u(t)$ on the trajectory in which the angle between vector field and normal to CTO section is the largest — see Figure 4.

Settings of the experiments are the same as in the case of fixed Poincaré section presented in Section 3.1. Our aim is to compute $z = B^{-1}(\mathcal{P}^2(X) - u)$, where $X = u + B \cdot r$, $r = \frac{1}{2}s \cdot (0, [-1, 1], \dots, [-1, 1])$ and $s > 0$ is the diameter of initial condition in the coordinate system B . In each case we run the Algorithm 6 with the matrix $A = B^{-1}$ as described in **diag+flowdir** strategy (29).

Results of experiment are partially listed in Tables 3, 4, 5 and 6 (columns orthogonal, CTO and max angle CTO) and visualised in Figure 5. We would like to emphasize, that these data cannot be compared directly to each other and to results from previous experiment in Section 3.1. Here Poincaré maps have different domains and we actually integrate different sets (perhaps of different initial area/volume).

We observe that for small and moderate sizes of sets, results from experiments involving **diag+flowdir** strategy, that is fixed section, orthogonal, CTO and max angle CTO sections, are comparable. All of them are very accurate and there is no room for large improvements.

For large sets we see that the results are significantly overestimated — see Figure 6. The main source of such errors comes from integration of quite large set over the period of the orbit. This leads to overestimation of $X_0 \supset \varphi(t_0, X)$ and in consequence to quite large enclosure on the main component of the result, that is $y_0 = \text{affineTransform}(X_0, A, y)$.

4. Conclusions

We proposed a new algorithm for efficient enclosing Poincaré maps. It takes advantage from the knowledge about representation of subsets of \mathbb{R}^n by the underlying ODE solver. We have shown, that in general situation proper choice of coordinate system, that is **flowdir** strategy, allows to reduce sliding and wrapping effects when a set of trajectories crosses the section. Numerical experiments show, that for small and moderate sizes of sets, obtained enclosures are very close to what is expected from linear approximation of Poincaré map.

A strategy for choosing Poincaré sections at approximate periodic points, described in section 3.4, minimizes diameter of crossing time. This allows further reduction of overestimation of $\mathcal{P}(X)$ for larger sets X . Although for large initial sets the main source of overestimation is a long time integration of ODE, our numerical findings in most of the cases indicate significant improvement given by CTO strategy when compared to the other ones.

The implementation of the algorithms presented in this paper are freely available as a part of the CAPD library [18, 19]. A serious test for the quality of implementation was a computer-assisted verification of chaos in infinite dimensional system (Kuramoto–Sivashinsky PDE) [33] or verification of hyperchaos [1, 34] in the 4D Rössler system.

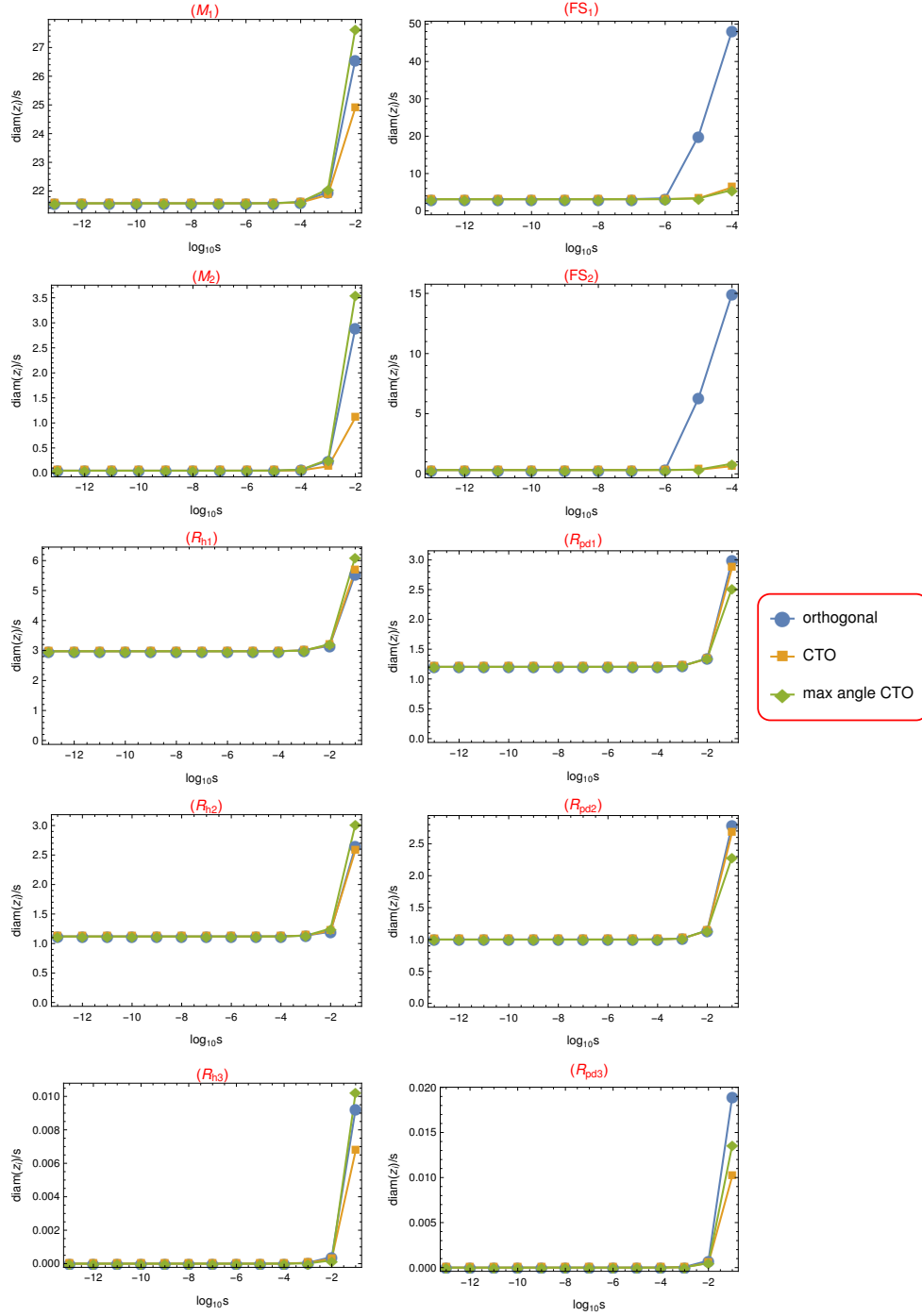


Figure 5: Comparison of enclosures of $z = B^{-1}(\mathcal{P}^2(u + B \cdot r) - u)$ computed by different methods. Horizontal axis corresponds to logarithms of size s of the initial set r . On vertical axis we plot the ratio $\text{diam}(z_i)/s$, which for small s should be close to the corresponding eigenvalue of $D\mathcal{P}^2(u)$.

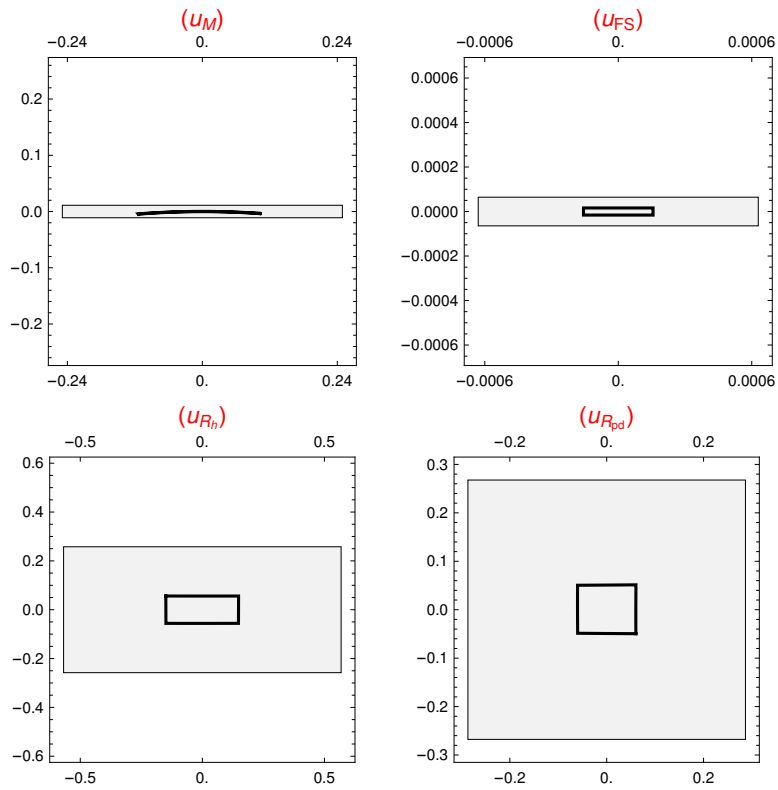


Figure 6: In grey – projection onto (z_2, z_3) of an enclosure of $z = B^{-1}(\mathcal{P}^2(u + B \cdot r) - u)$ onto two main coordinates computed for the largest size of r used in experiments — see CTO column in Tables 3, Table 4, Table 5 and Table 6. In black — an approximate shape of such projection computed by a non-rigorous routine. In the case of 4D Rössler system we skip the last z_4 coordinate which corresponds to strong contraction.

$\log_{10} s$	diag+normal	diag+flowdir	orthogonal	CTO	max angle CTO
$\lambda_{M_1} \approx -21.57189303583905$					
-13	22.288770093234	21.571893035879	21.571893035877	21.571893035868	21.571893035886
-12	22.288770093715	21.571893036244	21.571893036220	21.571893036127	21.571893036325
-11	22.288770098524	21.571893039893	21.571893039664	21.571893038726	21.571893040654
-10	22.288770146617	21.571893076394	21.571893074103	21.571893064721	21.571893083996
-9	22.288770627515	21.571893441397	21.571893418486	21.571893324667	21.571893517420
-8	22.288775436860	21.571897091434	21.571896862320	21.571895924126	21.571897851656
-7	22.288823530421	21.571933591888	21.571931300742	21.571921918754	21.571941194109
-6	22.289304477585	21.572298605637	21.572275692728	21.572181868412	21.572374627014
-5	22.294115104218	21.575949664009	21.575720389491	21.574781702701	21.576709794306
-4	22.342338639296	21.612552589485	21.610245257920	21.600813874537	21.620145477068
-3	22.836610909239	21.988082379753	21.963506140123	21.864579188760	22.064023271359
-2	28.684735372216	26.950444290822	26.572537443087	24.899391229219	27.640671971912
$\lambda_{M_2} \approx -0.046356617768258279$					
-13	16.134915640465	0.046356617787156	0.046356617784308	0.046356617774995	0.046356617788210
-12	16.134915640887	0.046356617957266	0.046356617928783	0.046356617835662	0.046356617967803
-11	16.134915645110	0.046356619658364	0.046356619373536	0.046356618442332	0.046356619763732
-10	16.134915687348	0.046356636669347	0.046356633821066	0.046356624509024	0.046356637723029
-9	16.134916109700	0.046356806779235	0.046356778296425	0.046356685175975	0.046356817316206
-8	16.134920333587	0.046358507884187	0.046358223056044	0.046357291848356	0.046358613269082
-7	16.134962572563	0.046375519540821	0.046372671255224	0.046363358859580	0.046376574908491
-6	16.135384972877	0.046545696834452	0.046517213563835	0.046424057719320	0.046556402492512
-5	16.139610031950	0.048253558313519	0.047968685063875	0.047033927584654	0.048375923353681
-4	16.181967982389	0.065957180118245	0.063105333370683	0.053427383868315	0.067766038947423
-3	16.616844425767	0.27530605365471	0.24486689683707	0.13335710379016	0.26868430398964
-2	21.778676674834	3.3796717087139	2.8985584015404	1.1081551960197	3.5608490573157

Table 3: Computed ratio $diam(z_i)/s$ for the orbit u_M . Columns **diag+normal** and **diag+flowdir** contain results of the experiment with fixed Poincaré section as described Section 3.1. Columns **orthogonal**, **CTO** and **max angle CTO** contain results of the experiment with varying sections as described in Section 3.4. Note that data in orthogonal, CTO and max angle CTO cannot be directly compared because these sections are different and thus we compute bound on Poincaré map on different sets.

$\log_{10} s$	diag+normal	diag+flowdir	orthogonal	CTO	max angle CTO
$\lambda_{FS_1} \approx -3.1255162015308699$					
-13	3.2116142444263	3.1255162038258	3.1255162269739	3.1255162039846	3.1255162077022
-12	3.2116142655580	3.1255162244797	3.1255164559613	3.1255162260679	3.1255162249376
-11	3.2116144768748	3.1255164310196	3.1255187458357	3.1255164469009	3.1255164321661
-10	3.2116165900434	3.1255184964189	3.1255416446378	3.1255186552321	3.1255185078836
-9	3.2116377217797	3.1255391504587	3.1257706385001	3.1255407385979	3.1255392650706
-8	3.2118490440011	3.1257456956048	3.1280611613276	3.1257615776825	3.1257468381526
-7	3.2139627521408	3.1278116218805	3.1510249035516	3.1279705113076	3.1278226902171
-6	3.2351484960973	3.1485184344710	3.3866083502860	3.1501142089676	3.1485933519525
-5	3.4519428524253	3.3604105774357	20.073719793613	3.3770717466865	3.3575308921411
-4	6.1918831644386	6.0382345907118	48.192050322691	6.2929366399838	5.5793036988113
$\lambda_{FS_2} \approx -0.31994714969328985$					
-13	0.58904797067828	0.31994714992826	0.31994715230733	0.31994714994447	0.31994715050329
-12	0.58904797368178	0.31994715204298	0.31994717583371	0.31994715220505	0.31994715370896
-11	0.58904800371685	0.31994717319017	0.31994741109760	0.31994717481089	0.31994718904359
-10	0.58904830406741	0.31994738466211	0.31994976374250	0.31994740086931	0.31994754319639
-9	0.58905130758169	0.31994949938640	0.31997329079895	0.31994966145907	0.31995108473517
-8	0.58908134341692	0.31997064711589	0.32020862211667	0.31997226791244	0.31998650120326
-7	0.58938177100241	0.32018217307783	0.32256802070380	0.32019838802569	0.32034077392439
-6	0.59239298018272	0.32230230643042	0.34678075911647	0.32246515567799	0.32389432028560
-5	0.62320851091933	0.34399811694236	6.3011376294349	0.34569814280737	0.36052693835901
-4	1.0129131821593	0.61828066926388	14.959060502378	0.64422908261053	0.84497758478011

Table 4: Computed ratio $diam(z_i)/s$ for the orbit u_{FS} . Columns **diag+normal** and **diag+flowdir** contain results of the experiment with fixed Poincaré section as described Section 3.1. Columns **orthogonal**, **CTO** and **max angle CTO** contain results of the experiment with varying sections as described in Section 3.4. Note that data in orthogonal, CTO and max angle CTO cannot be directly compared because these sections are different and thus we compute bound on Poincaré map on different sets.

$\log_{10} s$	diag+normal	diag+flowdir	orthogonal	CTO	max angle CTO
$\lambda_{R_{h_1}} \approx -2.9753618617896986$					
-13	3.1269112296727	2.9753618617987	2.9753618617991	2.9753618617973	2.9753618617953
-12	3.1269112296767	2.9753618618023	2.9753618618019	2.9753618618042	2.9753618618071
-11	3.1269112299772	2.9753618620903	2.9753618620850	2.9753618620637	2.9753618620608
-10	3.1269112327992	2.9753618647951	2.9753618647424	2.9753618645294	2.9753618645006
-9	3.1269112610131	2.9753618918436	2.9753618913169	2.9753618891866	2.9753618888981
-8	3.1269115432163	2.9753621623288	2.9753621570618	2.9753621357587	2.9753621328741
-7	3.1269143652214	2.9753648671818	2.9753648145118	2.9753646014813	2.9753645726348
-6	3.1269425854365	2.9753919158704	2.9753913891678	2.9753892588373	2.9753889703684
-5	3.1272248040375	2.9756624185652	2.9756571512700	2.9756358454017	2.9756329603539
-4	3.1300486358109	2.9783690272406	2.9783163272842	2.9781030120969	2.9780741257411
-3	3.1551299308307	3.0024276270455	3.0019370205452	3.0053562752534	3.0006911559382
-2	3.3312447246999	3.1612927762392	3.1579216074761	3.1824418580936	3.2139664668233
-1	5.9748947614907	5.5919232064410	5.5499757238534	5.6828287198362	6.1202554505770
$\lambda_{R_{h_2}} \approx 1.1193329361699592$					
-13	1.2750081236836	1.1193329361772	1.1193329361780	1.1193329361755	1.1193329361756
-12	1.2750081236814	1.1193329361751	1.1193329361749	1.1193329361760	1.1193329361771
-11	1.2750081238407	1.1193329363308	1.1193329363269	1.1193329362917	1.1193329363020
-10	1.2750081253204	1.1193329377781	1.1193329377391	1.1193329373876	1.1193329374899
-9	1.2750081401109	1.1193329522510	1.1193329518609	1.1193329483465	1.1193329493692
-8	1.2750082880882	1.1193330969806	1.1193330930796	1.1193330579353	1.1193330681626
-7	1.2750097678299	1.1193345442775	1.1193345052677	1.1193341538239	1.1193342560970
-6	1.2750245653503	1.1193490173467	1.1193486272464	1.1193451127757	1.1193461355106
-5	1.2751725508514	1.1194937580732	1.1194898568592	1.1194547088893	1.1194649366501
-4	1.2766534361840	1.1209421693982	1.1209031360826	1.1205513299068	1.1206536486960
-3	1.2904231607513	1.1343998401486	1.1340331850761	1.1369430453153	1.1333056956081
-2	1.3698919414549	1.2014426463159	1.1996643242106	1.2152067812507	1.2538154992768
-1	2.9997723907998	2.6705679634689	2.6493196773279	2.5783568485068	3.0211083048782

Table 5: Computed ratio $diam(z_i)/s$ for the orbit u_{R_h} . Columns **diag+normal** and **diag+flowdir** contain results of the experiment with fixed Poincaré section as described Section 3.1. Columns orthogonal, CTO and max angle CTO contain results of the experiment with varying sections as described in Section 3.4. Note that data in orthogonal, CTO and max angle CTO cannot be directly compared because these sections are different and thus we compute bound on Poincaré map on different sets.

$\log_{10} s$	diag+normal	diag+flowdir	orthogonal	CTO	max angle CTO
$\lambda_{R_{pd1}} \approx 1.2039286263296685$					
-13	1.3744854888330	1.2039286263323	1.2039286263322	1.2039286263322	1.2039286263316
-12	1.3744854888497	1.2039286263484	1.2039286263480	1.2039286263474	1.2039286263453
-11	1.3744854890396	1.2039286265322	1.2039286265287	1.2039286265228	1.2039286265000
-10	1.3744854909230	1.2039286283550	1.2039286283202	1.2039286282607	1.2039286280334
-9	1.3744855097563	1.2039286465824	1.2039286462353	1.2039286456404	1.2039286433675
-8	1.3744856980897	1.2039288288571	1.2039288253857	1.2039288194367	1.2039287967079
-7	1.3744875814245	1.2039306516056	1.2039306168909	1.2039305574015	1.2039303301127
-6	1.3745064136666	1.2039488792229	1.2039485320727	1.2039479371714	1.2039456642602
-5	1.3746947443819	1.2041311685904	1.2041276967474	1.2041217470111	1.2040990156302
-4	1.3764909757232	1.2058681783762	1.2058331605620	1.2057750473739	1.2056335194386
-3	1.3923461796892	1.2211702025606	1.2208174545532	1.2202191822506	1.2201485891365
-2	1.5245370044750	1.3482398006188	1.3444079718526	1.3378502373169	1.3452772133533
-1	3.3189752159528	3.0595461571246	2.9899841238967	2.8651359578762	2.5268610111985
$\lambda_{R_{pd2}} \approx -1$					
-13	1.1486171722293	1.0000000000020	1.0000000000020	1.0000000000019	1.0000000000015
-12	1.1486171722484	1.0000000000190	1.0000000000186	1.0000000000181	1.0000000000159
-11	1.1486171724575	1.0000000002049	1.0000000002015	1.0000000001971	1.0000000001738
-10	1.1486171745303	1.0000000020486	1.0000000020146	1.0000000019712	1.0000000017376
-9	1.1486171952589	1.0000000204855	1.0000000201457	1.0000000197118	1.0000000173756
-8	1.1486174025442	1.0000002048552	1.0000002014574	1.0000001971178	1.0000001737558
-7	1.1486194753993	1.0000020485537	1.0000020145757	1.0000019711789	1.0000017375590
-6	1.1486402030893	1.0000204856702	1.0000201458870	1.0000197119133	1.0000173756918
-5	1.1488474901282	1.0002048700441	1.0002014718711	1.0001971314897	1.0001737670547
-4	1.1508203440202	1.0019607036312	1.0019263987058	1.0018836409982	1.0017386848276
-3	1.1681410842692	1.0174040964627	1.0170577983291	1.0165945694829	1.0165327959562
-2	1.3108850142655	1.1452467277951	1.1414685208050	1.1359979815714	1.1438008444065
-1	3.2096656391944	2.8618925282316	2.7920556484803	2.6772944104801	2.2936430842608

Table 6: Computed ratio $diam(z_i)/s$ for the orbit $u_{R_{pd}}$. Columns **diag+normal** and **diag+flowdir** contain results of the experiment with fixed Poincaré section as described Section 3.1. Columns **orthogonal**, **CTO** and **max angle CTO** contain results of the experiment with varying sections as described in Section 3.4. Note that data in **orthogonal**, **CTO** and **max angle CTO** cannot be directly compared because these sections are different and thus we compute bound on Poincaré map on different sets.

References

- [1] R. Barrio, M. A. Martínez, S. Serrano, D. Wilczak, When chaos meets hyperchaos: 4d Rössler model, *Physics Letters A* 379 (38) (2015) 2300–2305. doi:<http://dx.doi.org/10.1016/j.physleta.2015.07.035>.
- [2] J. Cyranka, T. Wanner, Computer-assisted proof of heteroclinic connections in the one-dimensional Ohta–Kawasaki model, *SIAM Journal on Applied Dynamical Systems* 17 (1) (2018) 694–731. doi:[10.1137/17M111938X](https://doi.org/10.1137/17M111938X).
- [3] H. Kokubu, D. Wilczak, P. Zgliczyński, Rigorous verification of cocoon bifurcations in the Michelson system, *Nonlinearity* 20 (9) (2007) 2147–2174.
- [4] R. Szczelina, P. Zgliczyński, A homoclinic Orbit in a Planar Singular ODE—a computer assisted proof, *SIAM Journal on Applied Dynamical Systems* 12 (3) (2013) 1541–1565. doi:[10.1137/120901271](https://doi.org/10.1137/120901271).
- [5] D. Wilczak, The existence of Shilnikov homoclinic orbits in the Michelson system: A computer assisted proof, *Foundations of Computational Mathematics* 6 (4) (2006) 495–535. doi:[10.1007/s10208-005-0201-2](https://doi.org/10.1007/s10208-005-0201-2).
- [6] D. Wilczak, Abundance of heteroclinic and homoclinic orbits for the hyperchaotic Rössler system, *Discrete Contin. Dyn. Syst. Ser. B* 11 (4) (2009) 1039–1055.
- [7] D. Wilczak, P. Zgliczyński, Computer assisted proof of the existence of homoclinic tangency for the Hénon map and for the forced damped pendulum, *SIAM Journal on Applied Dynamical Systems* 8 (4) (2009) 1632–1663. doi:[10.1137/090759975](https://doi.org/10.1137/090759975).
- [8] W. Tucker, A rigorous ODE solver and Smale’s 14th problem, *Found. Comput. Math.* 2 (1) (2002) 53–117.
- [9] W. Tucker, Computing accurate poincaré maps, *Physica D: Nonlinear Phenomena* 171 (3) (2002) 127–137. doi:[https://doi.org/10.1016/S0167-2789\(02\)00603-6](https://doi.org/10.1016/S0167-2789(02)00603-6).
URL <https://www.sciencedirect.com/science/article/pii/S0167278902006036>
- [10] D. Wilczak, Uniformly hyperbolic attractor of the Smale–Williams type for a Poincaré map in the Kuznetsov system, *SIAM Journal on Applied Dynamical Systems* 9 (4) (2010) 1263–1283. doi:[10.1137/100795176](https://doi.org/10.1137/100795176).
- [11] D. Wilczak, R. Barrio, Systematic computer-assisted proof of branches of stable elliptic periodic orbits and surrounding invariant tori, *SIAM Journal on Applied Dynamical Systems* 16 (3) (2017) 1618–1649.
- [12] D. Wilczak, R. Barrio, Distribution of stable islands within chaotic areas in the non-hyperbolic and hyperbolic regimes in the Hénon–Heiles system, *Nonlinear Dynamics* (to appear).
- [13] M. Żelawski, Rigorous numerical approach to isolation in dynamical systems on the example of the Kuramoto–Sivashinsky equation, *Reliable Computing* 5 (2) (1999) 113–129. doi:[10.1023/A:1009945220181](https://doi.org/10.1023/A:1009945220181).
- [14] Z. Galias, On rigorous study of Poincaré maps defined by piecewise linear systems, in: *Proc. IEEE Int. Symp. Circuits Syst. (ISCAS)*, Kobe, Japan, 2005, pp. 3407–3410.
- [15] Z. Galias, Simulations of memristors using the Poincaré map approach, *IEEE Trans. Circuits Syst. I* 67 (3) (2020) 963–971. doi:[10.1109/TCSI.2019.2949736](https://doi.org/10.1109/TCSI.2019.2949736).
- [16] D. Ishii, K. Ueda, H. Hosobe, A. Goldsztejn, Interval-based solving of hybrid constraint systems, *IFAC Proceedings Volumes* 42 (17) (2009) 144–149, 3rd IFAC Conference on Analysis and Design of Hybrid Systems. doi:<https://doi.org/10.3182/20090916-3-ES-3003.00026>.
URL <https://www.sciencedirect.com/science/article/pii/S1474667015307527>
- [17] M. Konečný, W. Taha, F. Bartha, J. Duracz, A. Duracz, A. Ames, Enclosing the behavior of a hybrid automaton up to and beyond a zero point, *Nonlinear Analysis: Hybrid Systems* 20 (2016) 1–20. doi:<https://doi.org/10.1016/j.nahs.2015.10.004>.
URL <https://www.sciencedirect.com/science/article/pii/S1751570X15000606>
- [18] CAPD, Computer Assisted Proofs in Dynamics, a package for rigorous numerics, <http://capd.ii.uj.edu.pl>.
- [19] T. Kapela, M. Mrozek, D. Wilczak, P. Zgliczyński, CAPD::DynSys: a flexible C++ toolbox for rigorous numerical analysis of dynamical systems, *Communications in Nonlinear Science and Numerical Simulation* doi:[10.1016/j.cnsns.2020.105578](https://doi.org/10.1016/j.cnsns.2020.105578).
- [20] N. S. Nedialkov, VNODE-LP: A validated solver for initial value problems in ordinary differential equations, *Tech. Rep. Technical Report CAS-06-06-NN* (2006).
- [21] M. Berz, K. Makino, New methods for high-dimensional verified quadrature, *Reliable Computing* 5 (1) (1999) 13–22. doi:[10.1023/A:1026437523641](https://doi.org/10.1023/A:1026437523641).
- [22] M. Kashiwagi, kv - a c++ library for verified numerical computation (2019).
URL <http://verifiedby.me/kv/>
- [23] A. Rauh, M. Brill, C. Günther, A novel interval arithmetic approach for solving differential-algebraic equations with ValEncIA-IVP, *Int. J. Appl. Math. Comput. Sci.* 19 (3) (2009) 381–397. doi:[10.2478/v10006-009-0032-4](https://doi.org/10.2478/v10006-009-0032-4).
- [24] M. Mrozek, P. Zgliczyński, Set arithmetic and the enclosing problem in dynamics, *Ann. Polon. Math.* 74 (2000) 237–259.
- [25] T. Miyaji, P. Pilarczyk, M. Gameiro, H. Kokubu, K. Mischaikow, A study of rigorous ode integrators for multi-scale set-oriented computations, *Applied Numerical Mathematics* 107 (2016) 34–47. doi:<https://doi.org/10.1016/j.apnum.2016.04.005>.
URL <http://www.sciencedirect.com/science/article/pii/S0168927416300435>

- [26] R. E. Moore, Interval analysis, Prentice-Hall, Inc., Englewood Cliffs, N.J., 1966.
- [27] D. Michelson, Steady solutions of the Kuramoto-Sivashinsky equation, *Physica D: Nonlinear Phenomena* 19 (1) (1986) 89–111. doi:[http://dx.doi.org/10.1016/0167-2789\(86\)90055-2](http://dx.doi.org/10.1016/0167-2789(86)90055-2).
- [28] V. Falkner, S. Skan, Some approximate solutions of the boundary layer equations, *Phil. Mag.* 12 (1931) 865–896.
- [29] I. Walawska, D. Wilczak, Validated numerics for period-tupling and touch-and-go bifurcations of symmetric periodic orbits in reversible systems, *Communications in Nonlinear Science and Numerical Simulation* 74 (2019) 30–54. doi:<https://doi.org/10.1016/j.cnsns.2019.03.005>.
URL <http://www.sciencedirect.com/science/article/pii/S1007570419300735>
- [30] O. E. RöSSLer, An equation for hyperchaos, *Physics Letters A* 71 (2–3) (1979) 155–157.
- [31] N. S. Nedialkov, K. R. Jackson, An interval Hermite–Obreschkoff method for computing rigorous bounds on the solution of an initial value problem for an ordinary differential equation, *Developments in Reliable Computing* 5 (1998) 289–310.
- [32] L. Fousse, G. Hanrot, V. Lefèvre, P. PéLissier, P. Zimmermann, MPFR: A Multiple-Precision binary Floating-point library with correct Rounding, *ACM Trans. Math. Softw.* 33 (2) (2007) 13–es. doi:10.1145/1236463.1236468.
URL <https://doi.org/10.1145/1236463.1236468>
- [33] D. Wilczak, P. Zgliczyński, A geometric method for infinite-dimensional chaos: Symbolic dynamics for the Kuramoto-Sivashinsky PDE on the line, *Journal of Differential Equations* 269 (10) (2020) 8509–8548. doi:<https://doi.org/10.1016/j.jde.2020.06.020>.
URL <http://www.sciencedirect.com/science/article/pii/S002203962030334X>
- [34] D. Wilczak, S. Serrano, R. Barrio, Coexistence and dynamical connections between hyperchaos and chaos in the 4d rössler system: A computer-assisted proof, *SIAM Journal on Applied Dynamical Systems* 15 (1) (2016) 356–390. arXiv:<https://doi.org/10.1137/15M1039201>, doi:10.1137/15M1039201.
URL <https://doi.org/10.1137/15M1039201>